Waveguiding and correlated roughness effects in layered nanocomposite thin films studied by grazing-incidence small-angle x-ray scattering

D. Babonneau,* S. Camelio, D. Lantiat,† L. Simonot, and A. Michel
Laboratoire de Physique des Matériaux (PHYMAT), UMR 6630 CNRS, Université de Poitiers, SP2MI, Téléport 2, Bvd M. et P. Curie, BP 30179, 86962 Futuroscope Chasseneuil Cedex, France

(Received 23 February 2009; revised manuscript received 7 September 2009; published 23 October 2009)

Long-range interface correlations in C/Au/C and Ag/Si_3N_4 layered films consisting of metal nanoparticles embedded in amorphous matrices are investigated by atomic force microscopy, high-angle annular dark-field scanning transmission electron microscopy, x-ray reflectivity, and grazing-incidence small-angle x-ray scattering (GISAXS). We demonstrate that the GISAXS intensity of such systems is modulated by waveguiding and correlated roughness effects, which involve the use of a dynamical scattering theory to analyze the experimental data and to distinguish between both effects. Direct imaging methods and GISAXS experiments combined with quantitative analysis within the distorted wave-Born approximation thus provide complementary information. While no roughness correlation is observed in the C/Au/C trilayers, the surface roughness of the Si_3N_4 capping layers in the Ag/Si_3N_4 bilayers replicate the topography of the Ag nanoparticles resulting in a partial correlation, which decreases as the Si_3N_4 thickness increases.

DOI: 10.1103/PhysRevB.80.155446 PACS number(s): 68.35.Ct, 61.46.−w, 81.07.−b, 61.05.cf

I. INTRODUCTION

In recent years, investigations on nanoscale systems based on metal or semiconductor nanoparticles on solid surfaces have been motivated by their enormous potential for basic physics studies and device applications in many areas including magnetism, electronics, optics, catalysis, etc.[1] Modern deposition techniques make possible the synthesis of nanoparticles with uniform and controllable size, shape, and organization.[2] Very often, however, it is necessary to embed the nanoparticles in other materials, such as semiconductors or insulators, in order to study basic electronic properties, using *ex situ* measurements, or to achieve challenging technological goals. Therefore, increasing interest is now existing on the structure of nanoparticles embedded in matrices, i.e., nanoparticles that are capped after their formation under vacuum. In many cases, such capping yields an excellent passivation of the nanoparticle surface[3] as well as exceptional properties as hard and wear-resistant protective coatings[4] or biocompatible coatings for medical implants.[5] The matrix also plays a very important role in the physical properties of the system, which can be tuned by appropriate selection of the capping material. In addition, the capping process itself may induce drastic changes in size, shape, or composition of the nanoparticles associated, for example, with strain release, segregation, faceting, intermixing, or strain-enhanced diffusion.[6,7] The evolution of nanoparticle shape and size during deposition of a capping layer on top of previously grown nanoparticles has been studied extensively.[8–10] However, it has become evident that the nanoparticles and the capping material are mutually influenced.[10–12] Therefore, a clear-cut assessment of how the nanoparticles modify the electronic properties of the matrix is essential since it will affect the electronic properties of the buried nanoparticles. Likewise, as shown in Fig. 1, the surface roughness of the capping layer may replicate the topography of the nanoparticles resulting in a full or partial correlation.[13] Such a replication can be used to control the vertical organization of nanoparticles embedded in granular multilayers,[14,15] but it might also lead to an inefficient protective strength for very special technical application such as coatings in microelectronics or optics.[16]

Various techniques have been proven useful in studying capping effects as well as lateral and vertical correlations in rough layered systems. Direct imaging methods such as atomic force microscopy (AFM) and transmission electron microscopy (TEM) are applied to obtain information on the surface topography and on the nanoparticle morphology, but they are limited to small sample areas. In contrast, x-ray scattering measurements provide statistical information on a macroscopic scale associated with a good depth sensitivity.[12,17–21] However, these techniques require convenient approaches that can explain the distribution of scattered intensity in the reciprocal space, which may be modulated by interferences produced by waveguiding[22,23] or correlated roughness effects.[16] In this article, we report on the structural characterization of layered nanocomposite thin films consisting of Au and Ag nanoparticles covered by amorphous C and Si_3N_4 layers. We show that long-range interface correlations in layered films can be investigated by using a combination of AFM, high-angle annular dark-field scanning transmission electron microscopy (HAADF-STEM), x-ray reflectivity (XRR), and grazing-incidence small-angle x-ray scattering (GISAXS). In particular, we demonstrate that waveguiding interferences can be generated in C/Au/C trilayers deposited on a Ni buffer whereas replication of topography from the Ag nanoparticles to the Si_3N_4 capping-layer roughness is evidenced in Ag/Si_3N_4 trilayers. The paper is organized as follows: the GISAXS theory in the framework of the distorted wave-Born approximation[24,25] (DWBA) is presented in Sec. II; the experimental methods are described in Sec. III, and Sec. IV contains the analysis and the discussion of the results, which are summarized in Sec. V.

II. GISAXS THEORY

Let us consider a plane wave $E_0^-(\vec{r},t)=A_0^-(\vec{r})e^{i(\omega t-\tilde{k}_0^-\vec{r})}$ impinging on the surface ($z_1=0$) of a stratified medium consist-

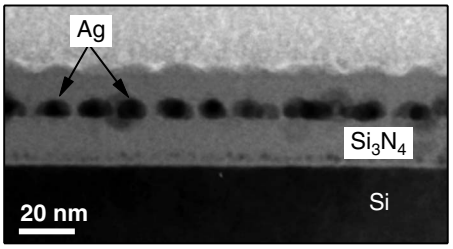

FIG. 1. Cross-sectional TEM image of Ag nanoparticles sandwiched between Si_3N_4 layers. The surface roughness of the Si_3N_4 capping layer replicates partially the topography of the Ag nanoparticles resulting in a lateral and vertical correlation.

ing of $N-1$ layers supported by a semi-infinite substrate, as illustrated in Fig. 2(a). The air and the substrate are labeled as medium 0 and N, respectively, and their refractive indices are $n_0=1$ and $n_N=1-\delta_N-i\beta_N$.[26] Each layer j $(1\leq j\leq N-1)$ is characterized by its refractive index $n_j=1-\delta_j-i\beta_j$ and its thickness t_j. The roughness of the interface z_j between the $j-1$ and j layers is σ_j. In the grazing-incidence geometry [Fig. 2(b)], the incident and scattered waves in air are described by wave vectors $\vec{k}_0^i$ and $\vec{k}_0^f$, which are defined by the angle of incidence (α_i) and by the in-plane $(2\theta_f)$ and out-of-plane (α_f) angles in emergence. The scattering vector in air $\vec{q}=(q_x,q_y,q_z)$ is then defined by

$$\vec{q}=\vec{k}_0^f-\vec{k}_0^i=\frac{2\pi}{\lambda}\begin{bmatrix}\cos(2\theta_f)\cos(\alpha_f)-\cos(\alpha_i)\\ \sin(2\theta_f)\cos(\alpha_f)\\ \sin(\alpha_f)+\sin(\alpha_i)\end{bmatrix}. \quad (1)$$

The incident and scattered waves propagating into the stratified medium are refracted and reflected at each interface so that the perpendicular component of the scattering vector in layer j is complex and defined by

$$\tilde{q}_{z,j}=\tilde{k}_{z,j}^f-\tilde{k}_{z,j}^i=\frac{2\pi}{\lambda}[\sqrt{n_j^2-\cos^2(\alpha_f)}+\sqrt{n_j^2-\cos^2(\alpha_i)}], \quad (2)$$

and the electric field intensity (EFI) in layer j is given by

$$|E_j(x,z)|^2=|[A_j^+(z_{j+1})e^{i\tilde{k}_{z,j}z}+A_j^-(z_{j+1})e^{-i\tilde{k}_{z,j}z}]e^{i(\omega t-k_{x,j}x)}|^2, \quad (3)$$

where $A_j^+(z_{j+1})$ and $A_j^-(z_{j+1})$ are the complex amplitudes of the upward and downward propagating waves at the interface z_{j+1} between the j and $j+1$ layers, which can be calculated by applying the Abeles matrix formalism.[26–29] The complex amplitude of the scattered wave by an object located at the interface z_{j+1} is then given by

$$\mathcal{A}_j^S(\mathbf{q})=\frac{k_0^2}{4\pi}(n_j^2-\nu_j^2)\Phi_j(\mathbf{q}), \quad (4)$$

where ν_j and $\Phi_j(\mathbf{q})$ are the refractive index and the form factor of the scattering object, respectively. In order to describe the grazing angle effects both in incidence and in emergence, the form factor can be expressed within the DWBA as[23,30–33]

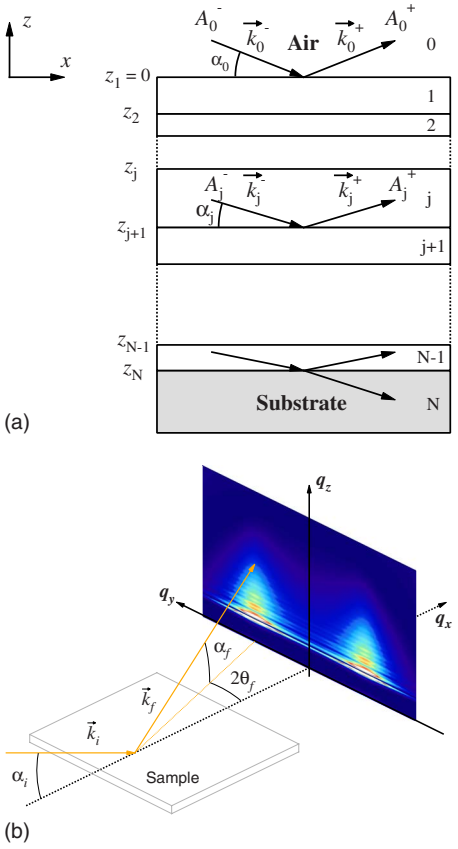

FIG. 2. (Color online) (a) Sketch of a plane wave propagating into a stratified medium. The z axis is perpendicular to the surface and its origin lies on the surface at $z_1=0$. The signs + (upward) and − (downward) label the direction of propagation of the wave. (b) Schematic drawing of the GISAXS geometry. α_i is the angle of incidence, while $2\theta_f$ and α_f are the in-plane and out-of-plane angles of emergence, respectively.

$$\begin{aligned}\Phi_j(q_\parallel,q_z)=&A_j^-(\alpha_i)A_j^-(\alpha_f)F_j(q_\parallel,\tilde{k}_{z,j}^f-\tilde{k}_{z,j}^i)\\&+A_j^+(\alpha_i)A_j^-(\alpha_f)F_j(q_\parallel,\tilde{k}_{z,j}^f+\tilde{k}_{z,j}^i)\\&+A_j^-(\alpha_i)A_j^+(\alpha_f)F_j(q_\parallel,-\tilde{k}_{z,j}^f-\tilde{k}_{z,j}^i)\\&+A_j^+(\alpha_i)A_j^+(\alpha_f)F_j(q_\parallel,-\tilde{k}_{z,j}^f+\tilde{k}_{z,j}^i),\end{aligned} \quad (5)$$

where $q_\parallel=\sqrt{q_x^2+q_y^2}$ is the in-plane component of the scattering vector and $F_j(q)$ is the Fourier transform of the shape of the object (i.e., its form factor calculated in the Born approximation).

In the case of a two-dimensional (2D) assembly of polydisperse scattering objects located at the interface z_{j+1}, the GISAXS intensity can be calculated in the framework of the local monodisperse approximation by assuming that the total polydisperse system consists of monodisperse subsystems:[34]

$$\mathcal{I}_j^S(\mathbf{q})=\int_0^\infty \mathcal{N}_j(D)\mathcal{S}_j(q_\parallel,D)|\mathcal{A}_j^S(\mathbf{q})|^2dD, \quad (6)$$

where $\mathcal{N}_j(D)$ is the size distribution function of the scattering objects and $\mathcal{S}_j(q_\parallel,D)$ is the structure factor due to the spatial correlation. At this stage, it is worth noting that modulations

of intensity can be generated in the q_z direction of the 2D GISAXS pattern resulting from interference between the upward and downward propagating waves (i.e., waveguiding effect close to the total external reflection).

Now, assuming that the GISAXS intensity originates from 2D assemblies located at two different interfaces, and that the lateral positions of the scattering objects located at the interface z_{j+1} are perfectly replicated to scattering objects located at the interface z_{k+1} $(k<j)$, the total scattered intensity is

$$\mathcal{I}^{S}_{tot}(\mathbf{q}) = \int_0^\infty \mathcal{N}_j(D)\mathcal{S}_j(q_{\parallel},D)|\mathcal{A}^{S}_{tot}(\mathbf{q})|^2 dD, \quad (7)$$

where $|\mathcal{A}^{S}_{tot}(\mathbf{q})|^2$ is the sum of three terms[35] describing (i) the intensity scattered by the objects located at the interface z_{j+1}, (ii) the intensity scattered by the objects located at the interface z_{k+1}, and (iii) the interference between them

$$|\mathcal{A}^{S}_{tot}(\mathbf{q})|^2 = |\mathcal{A}^{S}_{j}(\mathbf{q})|^2 + |\mathcal{A}^{S}_{k}(\mathbf{q})|^2 + 2|\mathcal{A}^{S}_{j}(\mathbf{q})||\mathcal{A}^{S}_{k}(\mathbf{q})|\cos[q_z(z_{j+1}-z_{k+1})]. \quad (8)$$

As a result of the cross term, modulations of intensity can be also generated in the q_z direction of the 2D GISAXS pattern with a well-defined period given by $\Delta q_z = 2\pi/(z_{j+1}-z_{k+1})$.[12,16,17,35]

III. EXPERIMENTAL METHOD

A. Sample preparation

Two C/Au/C and three Ag/Si_3N_4 layered nanocomposite thin films were deposited at 200 °C by ion-beam sputtering onto carbon-coated copper grids and naturally surface-oxidized Si(001) substrates. A first C/Au/C sample (labeled CAuC) was prepared by alternate sputtering of high-purity Au and C targets in order to produce a discontinuous layer of Au nanoparticles sandwiched between two amorphous carbon layers. The nominal thickness of the C buffer and capping layers was 17.5 nm, while the effective thickness of Au was 0.8 nm. To generate a waveguiding interference effect and to validate the theory described in Sec. II, another C/Au/C nanocomposite trilayer (labeled NiCAuC) was deposited onto a Ni buffer layer with a nominal thickness of 18 nm (the thicknesses of the Au and C capping-layer were not modified, while the thickness of the C buffer layer was reduced to 13 nm). In the case of the Ag/Si_3N_4 nanocomposite bilayers (labeled AS12, AS60, and AS120), the growth of the discontinuous layer of Ag nanoparticles (effective thickness of 3.6 nm) was performed directly onto the substrate without buffer layer. Subsequently, the Ag nanoparticles were covered with amorphous-Si_3N_4 capping layers of nominal thickness $t_{Si_3N_4}=12$ nm, $t_{Si_3N_4}=60$ nm, and $t_{Si_3N_4}=120$ nm, respectively. Moreover, in order to obtain the correct stoichiometry, the Si_3N_4 layers were irradiated, during deposition, by a 50 eV reactive nitrogen ion beam.

B. Structural characterization

XRR experiments were performed using the Cu-K_{α_1} radiation ($\lambda=0.154$ nm) with a four-circle x-ray diffractometer, equipped with a channel cut Ge(220) monochromator, to determine the thickness, roughness and density of the layers constituting the stratified samples. The RAYFLEX ANALYZE™ software (Rich. Seifert and Co.) was used to analyze the experimental data with an approach based on the Abeles matrix formalism,[26–29] and assuming a Gaussian height probability distribution. The morphology (size and shape) of the nanoparticles formed in the CAuC and AS12 samples deposited onto carbon-coated copper grids was investigated from in-plane views by HAADF-STEM performed in a JEOL 2200FS microscope operated at 200 kV (probe size of 0.7 nm and inner collection angle of 50 mrad). The surface topography of the Ag/Si_3N_4 nanocomposite bilayers was examined by AFM with a Nanoscope Digital instrument operated in tapping mode.

GISAXS experiments were performed under vacuum with the small-angle scattering setup of the D2AM beamline at the European Synchrotron Radiation Facility (Grenoble, France). The focus of the incident x-ray beam on the sample was 0.4 mm(H) × 0.1 mm(V) (Full Width at Half Maximum, FWHM) and the energies of 6.99 and 8 keV were selected to measure the C/Au/C trilayers and Ag/Si_3N_4 bilayers, respectively. The transmitted and specularly reflected beams were masked by a vertical beam stop, and the scattered intensity was collected with a 2D charge-coupled device (CCD) detector placed at 410 mm from the C/Au/C trilayers and at 1035 mm from the Ag/Si_3N_4 bilayers. Before quantitative analysis, raw data were corrected for the background and nonuniform sensitivity of the CCD. The experimental data were analyzed with a home-made package developed within the IGOR Pro analysis software (WaveMetrics, Inc.).

IV. RESULTS

A. C/Au/C nanocomposite trilayers

1. HAADF-STEM characterizations

Figure 3(a) shows a representative plan-view HAADF-STEM image of the CAuC sample. The gold layer consists of a polydisperse assembly of Au nanoparticles embedded in a light matrix. Quantitative analysis of such an image can be accomplished by a standard image thresholding procedure to determine the in-plane size histogram of the nanoparticles,[11] which was accurately fitted with a log-normal distribution function specified by the mean value, $\langle D\rangle=3.41$ nm, and the FWHM, $w_D=2.37$ nm, as displayed in Fig. 3(b). In addition, because the image intensity is proportional to the square of the atomic number and to the atomic column occupancy, HAADF-STEM analysis allows one to obtain reliable information about the height H of the individual embedded nanoparticles, with no need of a cross-section sample.[10] By assuming that the nanoparticles are hemispheroidal and by using the method described in Ref. 10, Fig. 3(c) shows that D and κH (κ designates an experimental HAADF constant, which depends on the illumination conditions) present a statistical dependence. Although H tends to saturate for $D>4$ nm, we performed as a first approximation a linear fit yielding $\kappa H = 8.22D + 62.7$, which can be expressed as

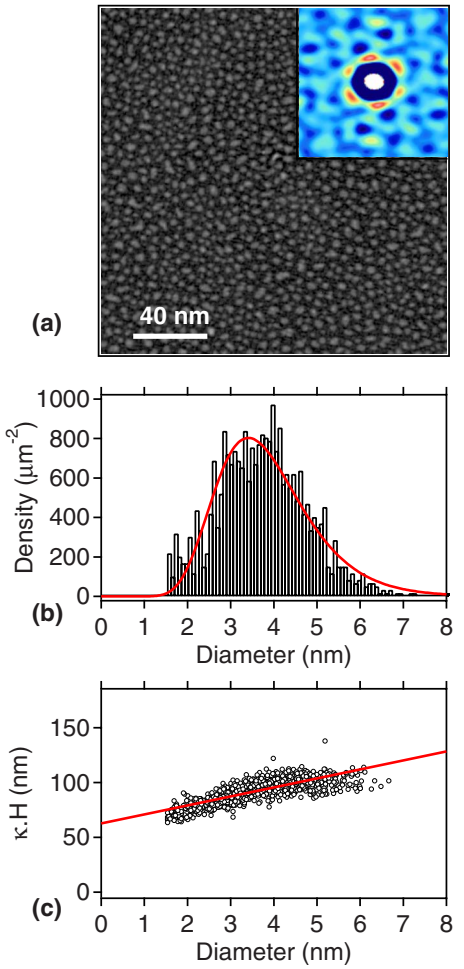

FIG. 3. (Color online) (a) Plan-view HAADF-STEM image (200×200 nm^2) of the CAuC sample and central part (40×40 nm^2) of the corresponding autocorrelation function (inset). (b) In-plane size distribution of the Au nanoparticles sandwiched between C layers. The solid line is a fit to a log-normal function specified by $\langle D\rangle=3.41$ nm and $w_D=2.37$ nm. (c) Correlation between the in-plane diameter D of the Au nanoparticles and their height H, with κ being an experimental constant. The solid line represents the best linear regression where the slope of the line is 8.22 and the y intercept is at 62.7 nm.

$$H = \frac{62.7}{\kappa}(0.131D + 1). \tag{9}$$

Also shown in Fig. 3(a) (inset) is the autocorrelation function (ACF) of the HAADF-STEM image, which is the cross-correlation of the image with itself. Although the particles have isotropic orientation and in-plane distribution at long distance (resulting in a circular ACF for larger images), the central part of this local ACF displays a pattern of dots with hexagonal symmetry. This result indicates a short-range ordering between nanoparticles with an average distance between nearest neighbors of $L_{TEM}=6.85$ nm, as estimated from the radial position of the dots.

2. XRR measurements and EFI distributions

Figure 4 shows the normalized reflectivity curves (i.e., $|A_0^+|^2/|A_0^-|^2$) for the CAuC and NiCAuC samples, which were

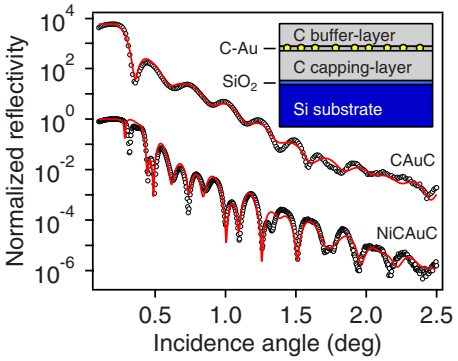

FIG. 4. (Color online) Normalized reflectivity curves of the C/Au/C nanocomposite trilayers measured using the Cu-K_{α_1} radiation ($\lambda=0.154$ nm) (symbols). The top inset gives a scheme of the stacking obtained from a fit to the experimental data (solid line) of the CAuC sample. The data of the CAuC sample have been shifted upward for clarity.

fitted by assuming a stratified medium consisting of a C-Au nanocomposite layer sandwiched between two amorphous carbon layers (inset). The Kiessig fringes expected in the curve of the CAuC sample are smeared out due to weak electron-density contrast between the C buffer layer and the Si substrate. In contrast, the data of the NiCAuC sample display several well-pronounced fringes with sharp reflection minima, which arise from the presence of the Ni mirrorlike layer of density 8.59 g/cm^3. For each layer of the stratified medium, the relevant parameters are the density, the thickness, and the interfacial roughness. Accordingly, a least-square fitting procedure was applied to refine the layer parameters, with the density and roughness of the Si substrate being fixed to 2.33 g/cm^3 and 0.1 nm, respectively. The roughness value of 0.1 nm, arbitrarily fixed for the Si substrate, is probably underestimated. However, the influence of this parameter (in the range 0.1 to 1 nm) on the simulated reflectivity is negligible. It should be also mentioned that the formalism used treats the C-Au nanocomposite layer like a homogeneous layer with a given density. Such a modeling certainly lacks accuracy, however the purpose of the XRR experiments is to get input values for further analysis of the GISAXS intensity, and this simple layered model is adequate to retrieve average parameters. The best-fit parameters obtained from the data collected for the CAuC and NiCAuC samples are reported in Tables I and II, respectively. Regarding the values extracted for the C-Au nanocomposite layer, it can be seen that the average thickness is around 2.6 nm (i.e., smaller than the average in-plane diameter $\langle D\rangle=3.41$ nm of the Au nanoparticles) and the average density is about 7.8 g/cm^3 thus corresponding to a C-Au volume composition of about 70–30 %. Furthermore, the roughness and density values of the C capping layer are higher than the corresponding values for the C buffer layer, which could indicate that the presence of the Au particles has an impact on the structure of the top carbon layer. However, this should be taken with care because several factors can lead to this result as Au contamination of the C capping layer as well as interlayer roughness not following a Gaussian distribution thus generating an error in the fitting. The simulation of the data

TABLE I. Parameters used to fit the x-ray reflectivity data of the CAuC sample shown in Fig. 4. The fixed parameters are indicated by the symbol #.

Layer	Material	Density (g/cm^3)	Thickness (nm)	Roughness (nm)
1	C	2.97 ± 0.10	13.3 ± 0.1	1.36 ± 0.14
2	C-Au	7.64 ± 0.08	2.61 ± 0.10	0.84 ± 0.08
3	C	2.33 ± 0.06	17.6 ± 0.1	0.57 ± 0.06
4	SiO_2	2.13 ± 0.03	2.17 ± 0.10	0.15 ± 0.02
5	Si	2.33#		0.10#

obtained for the NiCAuC sample yielded similar results by assuming an additional 18 nm-thick Ni layer between the native SiO_2 layer and the C buffer layer, suggesting that the presence of Ni does not modify the topography of the C-Au nanocomposite layer.

The EFI distributions [Eq. (3)], calculated at 6.99 keV by using the parameters deduced from the XRR best-fit values of the CAuC and NiCAuC samples, are shown as a function of the incidence angle α_i and depth z in Figs. 5(a) and 5(b). The difference in resonance modes between both samples is evident. While a EFI maximum of 3.25 is observed in the vicinity of the surface ($z_1=0$) of the CAuC sample at a grazing angle $\alpha_i=0.296°$ slightly smaller than the critical angle for total reflection ($\alpha_c=0.317°$), the EFI of the NiCAuC sample displays a significant enhancement, of about 13, located at $z \approx -20$ nm and $\alpha_i \approx 0.37°$. Also, compared to the CAuC sample [solid line in Fig. 5(a)], it can be clearly seen that the EFI at the location of the Au nanoparticles ($z=z_3$) in the NiCAuC sample [solid line in Fig. 5(b)] is greatly enhanced at $\alpha_i=0.37°$, but it collapses to almost 0 at $\alpha_i=0.41°$.

3. GISAXS analysis

The significance of such a waveguiding effect, which would increase or decrease the total GISAXS intensity proportionaly,[23] can be experimentally demonstrated by measuring 2D GISAXS patterns of the NiCAuC sample collected at $\alpha_i=0.370°$ [Fig. 6(a)] and at $\alpha_i=0.410°$ [Fig. 6(b)]. While the scattering signal measured with $\alpha_i=0.370°$ is typical of a 2D distribution of nanoparticles with a correlation peak only

TABLE II. Parameters used to fit the x-ray reflectivity data of the NiCAuC sample shown in Fig. 4. The fixed parameters are indicated by the symbol #.

Layer	Material	Density (g/cm^3)	Thickness (nm)	Roughness (nm)
1	C	3.02 ± 0.10	12.2 ± 0.1	1.31 ± 0.13
2	C-Au	7.99 ± 0.08	2.57 ± 0.10	0.94 ± 0.09
3	C	2.38 ± 0.06	12.7 ± 0.1	0.78 ± 0.08
4	Ni	8.59 ± 0.08	18.3 ± 0.1	0.69 ± 0.07
5	SiO_2	2.18 ± 0.03	1.59 ± 0.10	0.53 ± 0.05
6	Si	2.33#		0.10#

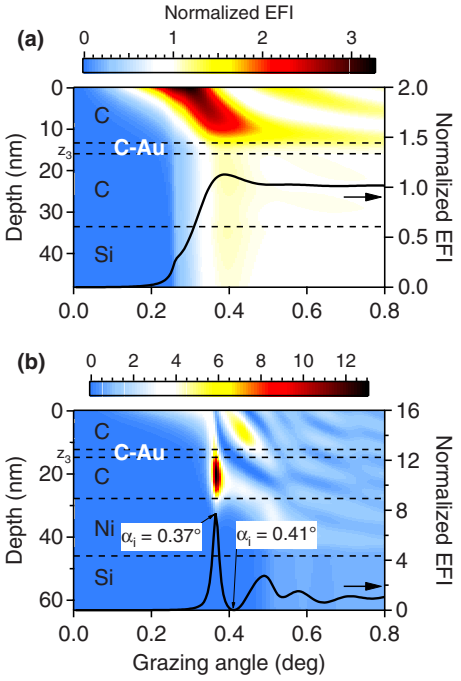

FIG. 5. (Color online) EFI distributions of the (a) CAuC and (b) NiCAuC samples, calculated at 6.99 keV by using the parameters deduced from the XRR fitting presented in Fig. 4. The solid lines represent the EFI (see right axis) as a function of the incidence angle α_i (calculated at the depth z_3) corresponding to the location of the Au nanoparticles.

in the lateral direction (parallel to q_y) at $2\theta_f \approx 1.60°$, it almost vanishes with $\alpha_i=0.410°$. In addition to the enhancement of the total scattered intensity, the GISAXS intensity measured with $\alpha_i=0.370°$ is also greatly enhanced at exit angles α_f equal to the incident angles at which waveguiding interference occurs in the thin film. As a consequence of the waveguiding interference of the scattered photons between the top and bottom interfaces of the C/Au/C nanocomposite trilayer, the GISAXS signal along the vertical direction (parallel to q_z) is modulated, which gives rise to sharp intensity fringes, as already reported by Narayanan *et al.* for Au nanoparticles embedded in a polymer-film-based waveguide.[23]

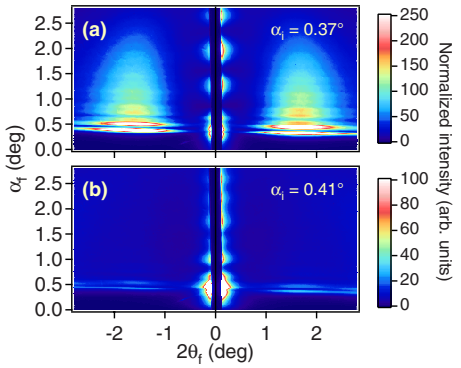

FIG. 6. (Color online) 2D GISAXS patterns of the NiCAuC sample measured at 6.99 keV with (a) $\alpha_i=0.370°$ and (b) $\alpha_i=0.410°$. The intensities were normalized to the number of incident photons.

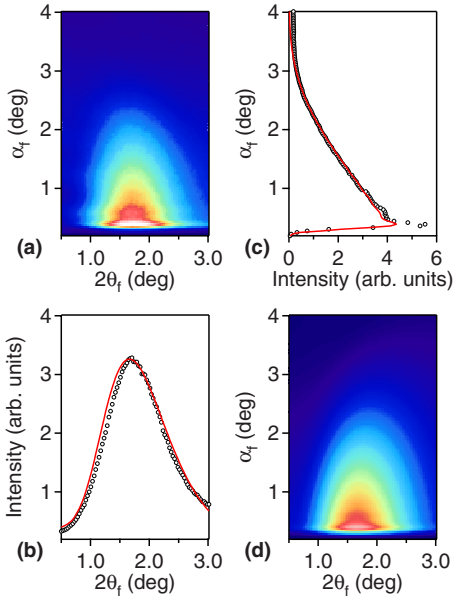

FIG. 7. (Color online) (a) Experimental 2D GISAXS pattern of the CAuC sample measured at 6.99 keV with α_i=0.480°. (b) Measured (symbols) and fitted (solid line) horizontal cross-sections drawn at α_f=1.00°. (c) Measured (symbols) and fitted (solid line) vertical cross sections drawn at $2\theta_f$=1.67°. (d) Simulated 2D GISAXS pattern using best-fit values.

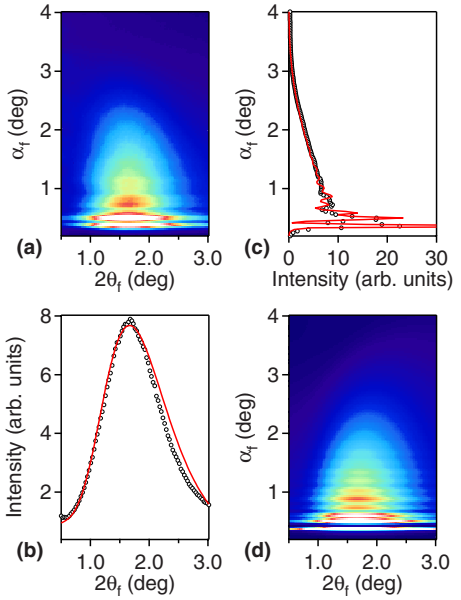

FIG. 8. (Color online) (a) Experimental 2D GISAXS pattern of the NiCAuC sample measured at 6.99 keV with α_i=0.535°. (b) Measured (symbols) and fitted (solid line) horizontal cross-sections drawn at α_f=1.00°. (c) Measured (symbols) and fitted (solid line) vertical cross-sections drawn at $2\theta_f$=1.67°. (d) Simulated 2D GISAXS pattern using best-fit values.

In order to obtain quantitative information on the shape and spatial arrangement of the Au nanoparticles, GISAXS measurements of the CAuC and NiCAuC samples were performed at grazing angles α_i=0.480° and α_i=0.535°, respectively, for which the EFI at the location of the Au nanoparticles is very close to unity. The experimental 2D GISAXS patterns, which were not sensitive to azimuthal rotation, are shown in Figs. 7(a) and 8(a). They illustrate the influence of the Ni-buffer layer on the modulation of the GISAXS signal along the q_z direction. The quantitative analysis of the GISAXS intensity was performed on the basis of four (one-dimensional) 1D cross sections drawn along a direction parallel to the surface plane at an exit angle $\alpha_f > 3\alpha_c$ (α_f =1.00°) and along the perpendicular direction at the position of the correlation peak ($2\theta_f$=1.67°). The corresponding cross-sectional scans, which are displayed in Figs. 7(b) and 7(c) and in Figs. 8(b) and 8(c), were simultaneously fitted using a Levenberg-Marquardt χ^2 criterion minimization,[36] by assuming that the surface roughness of the C/Au/C nanocomposite trilayers does not contribute to the total scattering signal [Eq. (6)]. The size distribution function of the scattering objects, $\mathcal{N}(D)$, was taken from the HAADF-STEM analysis and a linear correlation between the in-plane diameter D and the height H of the nanoparticles was imposed from Eq. (9). The structure factor, $\mathcal{S}(q_\parallel, D)$, was expressed analytically within the Percus-Yevick approximation for monodisperse hard spheres.[37] The hard-sphere diameter, D_{hs}, was assumed to be proportional to D with a constant factor C_{hs} ($D_{hs}=C_{hs}D$) and the hard-sphere volume fraction was η_{hs}.[34,38] In this analysis, the hard-sphere parameters, C_{hs} and η_{hs}, and the HAADF constant, κ, were used as fitting parameters. Then, 2D GISAXS patterns were calculated with the values obtained from the best fit, which are shown in Table III. As seen in Figs. 7(b)–7(d) and in Figs. 8(b)–8(d), the local monodisperse approximation assuming no correlated roughness shows an overall good agreement with the measured data for both samples. However, while the experimental 2D GISAXS patterns show scattering lobes oriented parallel to α_f or q_z, the simulated lobes are slightly inclined with the position of the correlation peak being shifted to higher $2\theta_f$ values as α_f is increased. This behavior can be interpreted as a consequence of the local monodisperse approximation (stating that the size of the scatterers and their positions are fully correlated) and of the linear relationship

TABLE III. Parameters used to fit the GISAXS data of the C/Au/C nanocomposite trilayers: normalized diameter ($C_{hs}=D_{hs}/D$) and volume fraction (η_{hs}) of the hard spheres, and HAADF constant (κ). Quantitative data derived from the combined HAADF-STEM and GISAXS analysis are also reported; interparticle distance (L_{TEM} and L_{SAXS}), mean value ($\langle H \rangle$) and FWHM (w_H) of the height distribution.

C_{hs}	η_{hs}	κ	L_{TEM} (nm)	L_{SAXS} (nm)	$\langle H \rangle$ (nm)	w_H (nm)
1.27	0.494	39.0	6.85	5.22	2.35	0.57

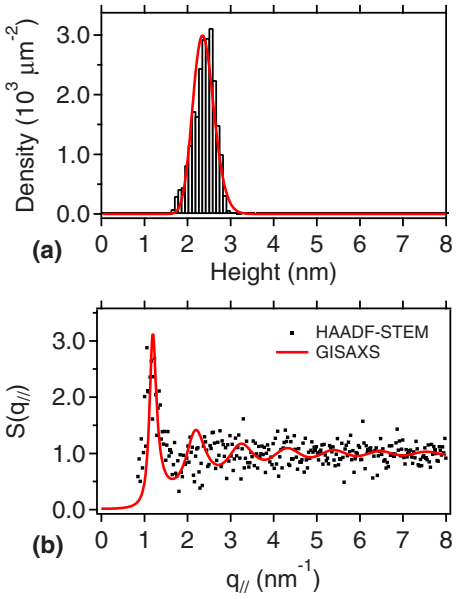

FIG. 9. (Color online) (a) Height distribution of the Au nanoparticles determined from the combined HAADF-STEM and GISAXS analyses. The solid line is a fit to a log-normal function specified by $\langle H\rangle$=2.35 nm and w_H=0.57 nm. (b) Structure factor calculated from the GISAXS fitting parameters (solid line) and obtained by Fourier transform of the pair correlation function deduced from the HAADF-STEM image displayed in Fig. 3 (symbols).

between the height and the diameter of the particles. Indeed, such a model implies that the correlation peak corresponding to the biggest particles is located at smaller q_y values than that corresponding to the smaller particles. Actually, it is likely that a different relationship between H and D including a saturation of H for $D>4$ nm associated to a size-spacing correlation approximation[39] should provide a better fitting of the whole GISAXS map. Nevertheless, these results confirm that the intensity modulation in the q_z direction of the 2D GISAXS patterns originates from a waveguiding interference effect and not from a correlation between the topography of the C-Au nanocomposite layer and the surface roughness. Accordingly, the HAADF constant κ can be estimated from the GISAXS analysis, and thus the height distribution of the Au nanoparticles can be deduced from Eq. (9). Figure 9(a) shows that the height distribution is smaller and narrower than the in-plane size distribution displayed in Fig. 3(b), and thus corresponds to Au nanoparticles with a spheroid shape and an average out-of-plane aspect ratio $\langle H\rangle/\langle D\rangle$ =0.69. This behavior, which has been already observed for metal nanoparticles formed by a Volmer-Weber growth mechanism,[11,39–42] most likely arises because the lateral growth of the nanoparticles is governed by complex processes including atom diffusion on the substrate and coalescence, whereas the vertical growth is driven mainly by direct deposition of atoms on the top of the particles.

Finally, the interparticle distance L_{SAXS}=5.22 nm was estimated from the position $q_{max}=2\pi/L_{SAXS}$ of the first maximum of the structure factor $\mathcal{S}(q_\parallel,\bar{D})$ [Fig. 9(b)] corresponding to Au particles with $\bar{D}=\Sigma_{i=1}^{N}D_i^4/\Sigma_{i=1}^{N}D_i^3$=4.57 nm (i.e., $\bar{D}$ is the D^3-weighted average diameter). As seen in Table III,

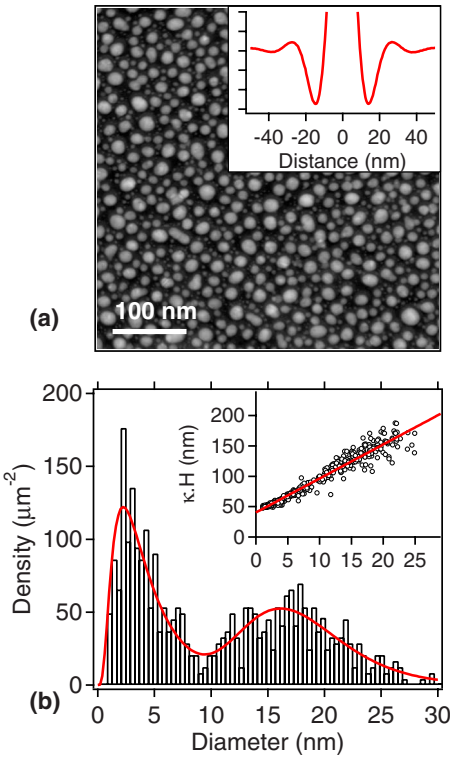

FIG. 10. (Color online) (a) Plan-view HAADF-STEM image of the AS12 sample and radial profile of the associated autocorrelation function (inset). (b) In-plane size distribution of the Ag nanoparticles capped with a 12 nm-Si_3N_4 layer. The solid line is a fit to a bimodal log-normal function. The correlation between the in-plane diameter D_{Ag} of the Ag nanoparticles and their height H_{Ag} is presented in the inset. The solid line represents the best linear regression where the slope of the line is 5.64 and the y intercept is at 39.7 nm.

L_{SAXS} is ~24% smaller than L_{TEM} determined from the ACF of the HAADF-STEM image of the CAuC sample [Fig. 3(a)]. However, Fig. 9(b) shows that there is a good agreement between $\mathcal{S}(q_\parallel,\bar{D})$ and the Fourier transform of $g(r)-1$, where $g(r)$ is the pair correlation function (related to the probability of finding the center of a particle at a given distance from the center of another particle) also determined from the HAADF-STEM image displayed in Fig. 3(a). As the pair correlation function depends only on the relative positions of the particles and not on their size, it can be concluded that L_{TEM} derived from the ACF of the HAADF-STEM image is overestimated due to particle-size effects (i.e., L_{TEM} reflects the distance between the larger particles of the distribution).

B. Ag/Si_3N_4 nanocomposite bilayers

1. HAADF-STEM and AFM characterizations

A representative plan-view HAADF-STEM image of the AS12 sample, consisting of Ag nanoparticles capped with a 12 nm-Si_3N_4 layer, is presented in Fig. 10(a). The interparticle distance estimated from the position of the first maximum of the associated ACF is L_{TEM}=27.3 nm (inset). Figure

10(b) shows that the in-plane size distribution is bimodal with a first peak centered at $D_1=2.25$ nm (FWHM, $w_1=4.23$ nm) and a second peak at $D_2=16.39$ nm ($w_2=10.34$ nm). This feature is commonly observed in the case of metal nanoparticles growing on insulating surfaces when the coalescence regime is established.[43–45] Moreover, as in the case of the Au nanoparticles sandwiched between C layers, the height H_{Ag} of the Ag nanoparticles shows a linear dependence with D_{Ag} (inset), which can be expressed as

$$H_{Ag}=\frac{39.7}{\kappa}(0.142D_{Ag}+1). \quad (10)$$

The AFM images of the Ag/Si_3N_4 nanocomposite bilayers with different capping thicknesses are displayed in Figs. 11(a)–11(c) together with the radial profiles of the corresponding ACFs (insets). The surface topography of the AS12 sample is characterized by the presence of islandlike nanostructures separated by a distance $L_{AFM}=34.0$ nm, as estimated from the position of the first maximum of the ACF indicated by the arrows in Fig. 11(a). Although 25% higher, this value is comparable to the distance $L_{TEM}=27.3$ nm determined by HAADF-STEM. This can suggest that the topography of the largest Ag nanoparticles is replicated at the surface of the bilayer, as already observed in $Si_3N_4/Ag/Si_3N_4$ trilayers from TEM cross-section views (Fig. 1).[11,13] However, when the nominal Si_3N_4 thickness is increased to $t_{Si_3N_4}=60$ nm [Fig. 11(b)], although islandlike nanostructures are still present on the surface, the distance between them increases to $L_{AFM}=36.9$ nm and the root-mean-square roughness decreases from $\sigma_{AFM}=1.89$ nm to $\sigma_{AFM}=1.12$ nm. For $t_{Si_3N_4}=120$ nm [Fig. 11(c)], the islands almost disappear with an interisland distance reaching $L_{AFM}=49.6$ nm, and the top surface of the bilayer is fairly flat with $\sigma_{AFM}=0.66$ nm.

2. XRR measurements and EFI distributions

Figure 12(a) shows the normalized reflectivity curves of the Ag/Si_3N_4 nanocomposite bilayers. Both the AS60 and AS120 samples display well-defined Kiessig fringes with a period inversely proportional to the thickness of the Si_3N_4 capping-layer, $t_{Si_3N_4}$. The smoothing of the Kiessig fringes observed for the AS12 sample can be explained by the presence of islandlike nanostructures, which induce an increase in the surface roughness, σ_{XRR}. The three curves were simultaneously fitted by assuming that all the parameters were identical from one sample to another, with the exception of the thickness and roughness of the Si_3N_4 capping layer (layer $j=1$). The best-fit parameters are gathered in Table IV and confirm that σ_{XRR} decreases when $t_{Si_3N_4}$ increases. In addition, the average thickness of the Si_3N_4-Ag nanocomposite layer is found around 6.7 nm and its roughness is 2.1 nm, similar to that of the Si_3N_4 layer covering the AS60 sample. The EFIs calculated at the location of the Ag nanoparticles as a function of the incidence angle, α_i, are presented in Fig. 12(b). Similar features are observed for the three samples: the EFI remains close to zero when α_i is smaller than the critical angle $\alpha_c=0.269°$, then it increases steeply at the critical angle, and finally it tends toward unity when $\alpha_i \gg \alpha_c$. It is also worth noting that a waveguiding interference effect causes weak oscillations of the EFI, as clearly observed in the case of the AS60 and AS120 samples. However, such modulations appear only for small grazing-angle values ($\alpha_i < 0.6°$) and the spacing of the fringes corresponds to $\Delta q_z = \pi/t_{Si_3N_4}$. Accordingly, the waveguiding effect can easily be distinguished from the roughness-correlation effect described in Sec. II because they differ in their wavelength.[16]

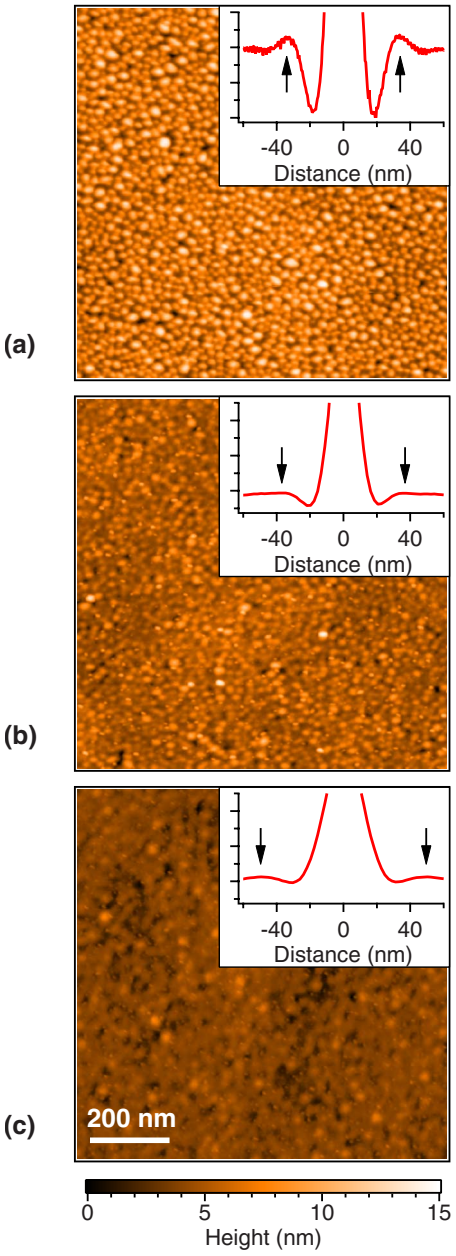

FIG. 11. (Color online) AFM images of the (a) AS12, (b) AS60, and (c) AS120 samples. The top right insets represent the radial profile of the autocorrelation functions of the AFM images. The positions of the first maxima of the ACFs are indicated by the arrows.

3. GISAXS analysis

Figures 13(a)–13(c) display the 2D GISAXS patterns of the Ag/Si_3N_4 nanocomposite bilayers measured at α_i

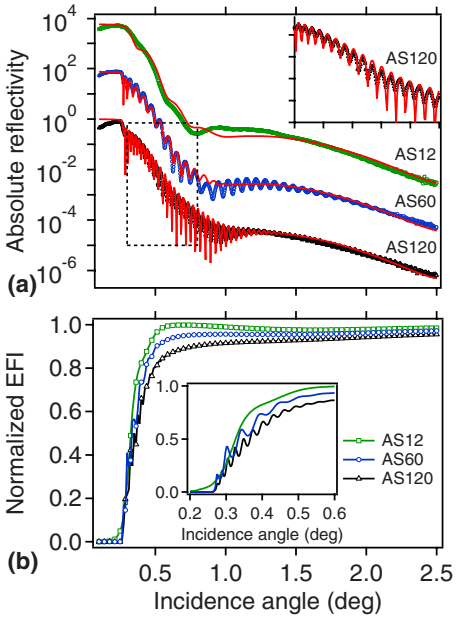

FIG. 12. (Color online) (a) Normalized reflectivity curves of the Ag/Si_3N_4 nanocomposite bilayers measured using the Cu-K_{α_1} radiation ($\lambda=0.154$ nm) (symbols). The solid lines correspond to the fitting used to determine the parameters reported in Table IV. The data of the AS12 and AS60 samples have been shifted upward for the sake of clarity. The top inset shows a magnification of the area delimited by the dotted rectangle (AS120 sample). (b) EFI as a function of the incidence angle α_i (calculated at 8 keV and at the location of the Ag nanoparticles, $z_3=-t_{Si_3N_4}$), for the Ag/Si_3N_4 nanocomposite bilayers by using the fitting parameters deduced from the XRR measurements.

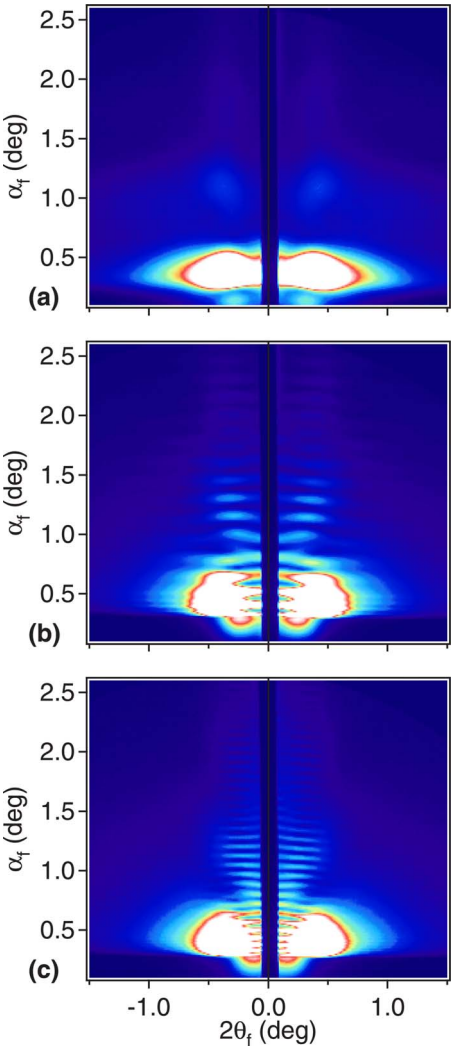

FIG. 13. (Color online) 2D GISAXS patterns of the Ag/Si_3N_4 nanocomposite bilayers measured at 8 keV with $\alpha_i=0.440°$: (a) AS12, (b) AS60, and (c) AS120 samples.

$=0.440°$. At least for the AS60 and AS120 samples, it is obvious that the intensity is concentrated in periodic stripes, which are straight and parallel to the q_y direction. The horizontal cross sections drawn at $\alpha_f=0.48°$ are very similar for the three samples [Figs. 14(a)–14(c)], and determine both the lateral form factor and the structure factor of the nanoparticles as in the case of the C/Au/C nanocomposite trilayers [Figs. 7(b) and 8(b)]. In contrast, the vertical cross-sections drawn at the position of the correlation peak, $2\theta_f=0.36°$ [Figs. 15(a)–15(c)], reveal intensity oscillations, which extend even far from the total external reflection region and are spaced out by a well-defined period corresponding to $\Delta q_z = 2\pi/t_{Si_3N_4}$. These results confirm that the islandlike nanostructures observed by AFM are well localized with respect to the nanoparticle positions since such an interference effect can occur only if the phase shift between the waves scattered by the Si_3N_4 islandlike nanostructures ($z_1=0$) and those scattered by the Ag nanoparticles ($z_3=-t_{Si_3N_4}$) is well-defined.[17,35] In addition, it is worth noting that inclined lobes are observed in the 2D GISAXS patterns of the

TABLE IV. Parameters used to fit the x-ray reflectivity data of the Ag/Si_3N_4 nanocomposite bilayers shown in Fig. 12(a). The fixed parameters are indicated by the symbol #.

Layer	Material	Density (g/cm^3)		Thickness (nm)	Roughness (nm)
1	Si_3N_4	3.29 ± 0.06	AS12→	11.83 ± 0.10	2.32 ± 0.23
			AS60→	56.39 ± 0.10	2.11 ± 0.21
			AS120→	112.7 ± 0.1	1.41 ± 0.14
2	Si_3N_4-Ag	7.16 ± 0.09		6.73 ± 0.10	2.10 ± 0.21
3	SiO_2	3.56 ± 0.05		2.44 ± 0.10	0.57 ± 0.06
4	Si	$2.33^{\#}$			$0.10^{\#}$

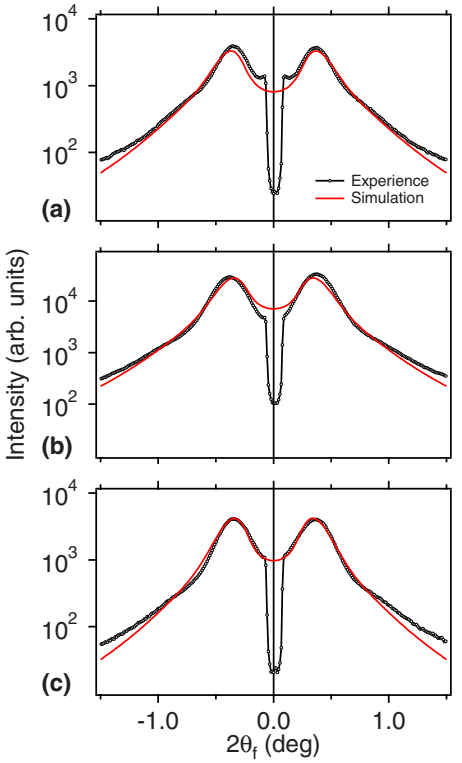

FIG. 14. (Color online) Measured (symbols) and fitted (solid lines) horizontal cross sections drawn at α_f=0.48° from the 2D GISAXS patterns of the (a) AS12, (b) AS60, and (c) AS120 samples.

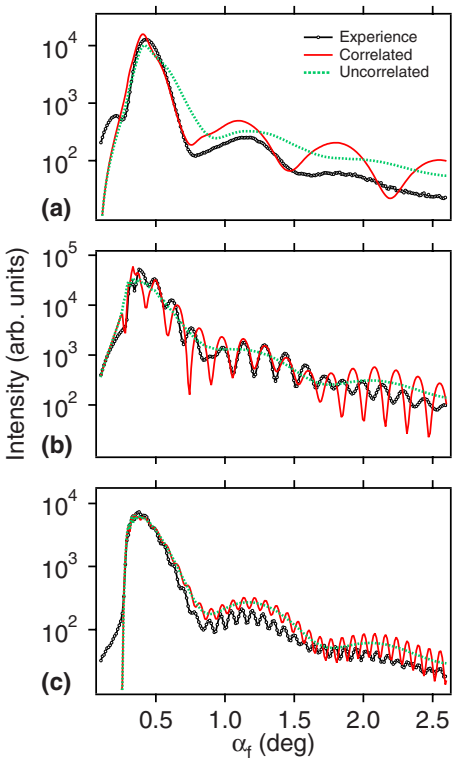

FIG. 15. (Color online) Measured (symbols) and fitted (solid lines) vertical cross-sections drawn at $2\theta_f$=0.36° from the 2D GISAXS patterns of the (a) AS12, (b) AS60, and (c) AS120 samples. Simulations by assuming no correlation between Ag nanoparticles and surface roughness (dotted lines) are also presented for comparison.

Ag/Si_3N_4 nanocomposite bilayers. As explained in Sec. IV A 3, these inclined lobes should not be misinterpreted as an effect of scattering from faceted particles, but can be ascribed to the statistical dependence of the particle diameter and height.[39]

The quantitative analysis of the GISAXS intensity was performed from Eqs. (7) and (8) by applying the same procedure as described in Sec. IV A 3 (i.e., the size distribution function of the Ag nanoparticles, $\mathcal{N}(D_{Ag})$, as well as the linear correlation between the in-plane diameter D_{Ag} and the height H_{Ag} were obtained from the HAADF-STEM analysis and the structure factor, $\mathcal{S}(q_{\parallel},D_{Ag})$, was expressed within the Percus-Yevick approximation). To simplify the model, the Si_3N_4 islandlike nanostructures were taken as hemispheroids with diameter $D_{Si_3N_4}=D_{Ag}$ and height $H_{Si_3N_4}=\xi_z H_{Ag}$, where ξ_z describes the degree of vertical correlation between Ag nanoparticles and surface roughness (Fig. 16). The six 1D cross-sectional scans displayed in Figs. 14(a)–14(c) and in Figs. 15(a)–15(c) were simultaneously fitted using C_{hs}, η_{hs}, κ, and ξ_z as free parameters (Table V). It should be noted that in this crude model, a perfect lateral replication between the Ag nanoparticles and the Si_3N_4 roughness is assumed. It is thus likely that better fits could be obtained by introducing an additional term describing the degree a lateral correlation. Nevertheless, a fairly good agreement between the experimental and simulated data was obtained with C_{hs}=1.10, η_{hs}=0.412, κ=16.11, and ξ_z=0.68 for AS12, ξ_z=0.59 for AS60, and ξ_z=0.02 for AS120. It is also worth noting in Fig. 15 that the vertical oscillations are not reproduced when assuming no correlation between Ag nanoparticles and surface roughness [i.e., by calculating the scattered intensity with the same parameters, but using only the two first terms of Eq. (8)]. It is thus obvious that (i) the modulations of the GISAXS intensity along the q_z direction are not generated by a waveguiding effect as in the case of the NiCAuC sample, (ii) the topography of the Ag nanoparticles is partially replicated at the surface of the Ag/Si_3N_4 nanocomposite trilayers, and (iii) the degree of vertical correlation decreases when $t_{Si_3N_4}$ increases.

Finally, the quantitative data presented in Table V also show that the height distribution of the Ag nanoparticles is smaller and narrower than the in-plane size distribution, similar to the case of the Au nanoparticles sandwiched be-

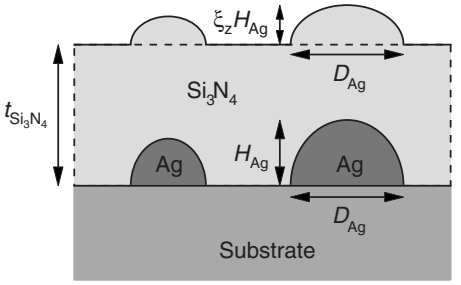

FIG. 16. Schematic drawing of a Ag/Si_3N_4 nanocomposite bilayer with partially correlated surface roughness.

TABLE V. Parameters used to fit the GISAXS data of the Ag/Si_3N_4 nanocomposite bilayers: normalized diameter ($C_{hs}=D_{hs}/D$) and volume fraction (η_{hs}) of the hard spheres, HAADF constant (κ), and degree of vertical correlation between Ag nanoparticles and surface roughness (ξ_z). Quantitative data derived from the combined AFM, HAADF-STEM and GISAXS analysis are also reported: interparticle distance (L_{AFM}, L_{TEM} and L_{SAXS}), mean value ($\langle H_{Ag}\rangle$) and FWHM (w_H) of the height distribution, and mean height of the Si_3N_4 islandlike nanostructures ($\langle H_{Si_3N_4}\rangle$).

Sample	C_{hs}	η_{hs}	κ	ξ_z	L_{AFM} (nm)	L_{TEM} (nm)	L_{SAXS} (nm)	$\langle H_{Ag}\rangle$ (nm)	w_H (nm)	$\langle H_{Si_3N_4}\rangle$ (nm)
AS12				0.68	34.0	27.3				5.34
AS60	1.10	0.412	16.11	0.59	36.9		21.5	7.85	3.52	4.63
AS120				0.02	49.6					0.16

tween C layers. Furthermore, the corresponding average heights of the Si_3N_4 islandlike nanostructures are $\langle H_{Si_3N_4}\rangle = 5.34$ nm, $\langle H_{Si_3N_4}\rangle = 4.63$ nm, and $\langle H_{Si_3N_4}\rangle = 0.16$ nm for the AS12, AS60, and AS120 samples, respectively, which is consistent with the decrease in the roughness observed both by XRR and AFM. Accordingly, although correlated roughness is still detected by GISAXS, the decrease of $\langle H_{Si_3N_4}\rangle$ may be the cause of the decrease in the island areal density seen by AFM, which induces an increase in the apparent interisland distance, L_{AFM}. Moreover, our results confirm that the interparticle distance, L_{SAXS}, estimated from the position of the first maximum of the structure factor $\mathcal{S}(q_\parallel, \bar{D}_{Ag})$ is smaller than L_{TEM} determined by HAADF-STEM, which is overestimated due to particle-size effects.

V. CONCLUSION

We have investigated in detail the nanostructure of C/Au/C and Ag/Si_3N_4 layered films consisting of metal nanoparticles embedded in amorphous matrices. We show that reliable information on lateral and vertical correlations can be obtained by combining HAADF-STEM, XRR, and GISAXS measurements associated with quantitative data analysis within the DWBA: while AFM gives only a direct image of the surface topography, and plan-view HAADF-STEM provides information on the morphology of the buried nanoparticles, GISAXS is sensitive to the lateral correlations between nanoparticles as well as vertical correlations between the nanoparticles and the surface with a statistical averaging. The theory presented in Sec. II can explain waveguiding effects observed in the NiCAuC layered film as well as correlated roughness effects in the Ag/Si_3N_4 bilayers. It is demonstrated that no roughness correlation is present in the C/Au/C trilayers whereas the surface of the Si_3N_4 capping layers tends to replicate the topography of the Ag nanoparticles. Although the degree of vertical correlation strongly decreases when the Si_3N_4 thickness increases, these correlations play a crucial role in the distribution of scattered intensity in the reciprocal space, which suggests that the lateral positions of the Ag nanoparticles are perfectly replicated at the surface of the Si_3N_4 capping layer even for $t_{Si_3N_4}$ as large as 120 nm (i.e., for $t_{Si_3N_4} \approx 15\langle H_{Ag}\rangle$). Further investigations are required to understand the mutual influence of the nanoparticles and the surrounding matrix. Nevertheless, with respect to the applications of such nanocomposite thin films, we found that both the nature and the thickness of the capping layer have an impact on the roughness correlations.

ACKNOWLEDGMENTS

We acknowledge the assistance of J.-P. Simon and of the D2AM technical staff during the GISAXS experiments. We thank M. Drouet and P. Guérin for assistance in the sample preparation.

*david.babonneau@univ-poitiers.fr
†Present address: Laboratoire de Chimie de la Matière Condensée de Paris, Université P. et M. Curie–Paris 6/CNRS–UMR 7574/ENSCP, France.

[1] G. Schmid, *Nanoparticles: From Theory to Application* (Wiley-VCH Verlag GmbH & Co. KGaA, Weinheim, 2004).
[2] N. Weiss *et al.*, Phys. Rev. Lett. **95**, 157204 (2005).
[3] N. Jaouen, D. Babonneau, J. M. Tonnerre, D. Carbone, F. Wilhelm, A. Rogalev, T. K. Johal, and G. van der Laan, Phys. Rev. B **76**, 104421 (2007).
[4] D. Babonneau, T. Cabioc'h, A. Naudon, J. C. Girard, and M. F. Denanot, Surf. Sci. **409**, 358 (1998).
[5] G. Francz, A. Schroeder, and R. Hauert, Surf. Interface Anal. **28**, 3 (1999).
[6] P. Sutter and M. G. Lagally, Phys. Rev. Lett. **81**, 3471 (1998).
[7] G. Costantini, A. Rastelli, C. Manzano, P. Acosta-Diaz, R. Songmuang, G. Katsaros, O. G. Schmidt, and K. Kern, Phys. Rev. Lett. **96**, 226106 (2006).
[8] A. Rastelli, M. Kummer, and H. von Känel, Phys. Rev. Lett. **87**, 256101 (2001).
[9] C. Lang, S. Kodambaka, F. M. Ross, and D. J. H. Cockayne, Phys. Rev. Lett. **97**, 226104 (2006).
[10] D. Lantiat, D. Babonneau, S. Camelio, F. Pailloux, and M.-F. Denanot, J. Appl. Phys. **102**, 113518 (2007).
[11] J. Toudert, S. Camelio, D. Babonneau, M.-F. Denanot, T. Girardeau, J. P. Espinos, F. Yubero, and A. R. Gonzalez-Elipe, J. Appl. Phys. **98**, 114316 (2005).
[12] J. Coraux, H. Renevier, V. Favre-Nicolin, G. Renaud, and B.

Daudin, Appl. Phys. Lett. **88**, 153125 (2006).
[13] S. Camelio, J. Toudert, D. Babonneau, and T. Girardeau, Appl. Phys. B: Lasers Opt. **80**, 89 (2005).
[14] A. Naudon, D. Babonneau, F. Petroff, and A. Vaurès, Thin Solid Films **319**, 81 (1998).
[15] D. Babonneau, G. Abadias, J. Toudert, T. Girardeau, E. Fonda, J. S. Micha, and F. Petroff, J. Phys.: Condens. Matter **20**, 035218 (2008).
[16] M. Kashem, J. Perlich, L. Schulz, S. Roth, and P. Muller-Buschbaum, Macromolecules **41**, 2186 (2008).
[17] V. Holý and T. Baumbach, Phys. Rev. B **49**, 10668 (1994).
[18] I. Kegel, T. H. Metzger, J. Peisl, J. Stangl, G. Bauer, and D. Smilgies, Phys. Rev. B **60**, 2516 (1999).
[19] A. Hesse, J. Stangl, V. Holý, T. Roch, G. Bauer, O. G. Schmidt, U. Denker, and B. Struth, Phys. Rev. B **66**, 085321 (2002).
[20] A. P. Payne and B. M. Clemens, Phys. Rev. B **47**, 2289 (1993).
[21] D. R. Lee, S. K. Sinha, C. S. Nelson, J. C. Lang, C. T. Venkataraman, G. Srajer, and R. M. Osgood, Phys. Rev. B **68**, 224410 (2003).
[22] J. Wang, M. Bedzyk, and M. Caffrey, Science **258**, 775 (1992).
[23] S. Narayanan, D. R. Lee, R. S. Guico, S. K. Sinha, and J. Wang, Phys. Rev. Lett. **94**, 145504 (2005).
[24] S. K. Sinha, E. B. Sirota, S. Garoff, and H. B. Stanley, Phys. Rev. B **38**, 2297 (1988).
[25] M. Rauscher, T. Salditt, and H. Spohn, Phys. Rev. B **52**, 16855 (1995).
[26] A. Gibaud, *X-ray and Neutron Reflectivity: Principles and Applications* (Springer, Paris, 1999).
[27] F. Abélès, Ann. Phys. (Paris) **5**, 596 (1950).
[28] L. G. Parratt, Phys. Rev. **95**, 359 (1954).
[29] M. Born and E. Wolf, *Principle of Optics* (Pergamon, London, 1959).
[30] B. Lee, J. Yoon, W. Oh, Y. Hwang, K. Heo, K. Jin, J. Kim, K.-W. Kim, and M. Ree, Macromolecules **38**, 3395 (2005).
[31] P. Busch, M. Rauscher, D.-M. Smilgies, D. Posselt, and C. M. Papadakis, J. Appl. Crystallogr. **39**, 433 (2006).
[32] H. Yokoyama, C. Dutriez, L. Li, T. Nemoto, K. Sugiyama, S. Sasaki, H. Masunaga, M. Takata, and H. Okuda, J. Chem. Phys. **127**, 014904 (2007).
[33] J. Mane Mane, C. S. Cojocaru, A. Barbier, J.-P. Deville, B. Thiodjio Sendja, and F. Le Normand, Phys. Status Solidi A **204**, 4209 (2007).
[34] J. S. Pedersen, J. Appl. Crystallogr. **27**, 595 (1994).
[35] F. Leroy, G. Renaud, A. Letoublon, R. Lazzari, C. Mottet, and J. Goniakowski, Phys. Rev. Lett. **95**, 185501 (2005).
[36] W. H. Press, B. P. Flannery, S. A. Teukolski, and W. T. Vetterling, *Numerical Recipes in C* (Cambridge University Press, New York, 1992).
[37] J. K. Percus and G. J. Yevick, Phys. Rev. **110**, 1 (1958).
[38] D. Babonneau, F. Pailloux, J.-P. Eymery, M.-F. Denanot, P. Guerin, E. Fonda, and O. Lyon, Phys. Rev. B **71**, 035430 (2005).
[39] R. Lazzari, G. Renaud, J. Jupille, and F. Leroy, Phys. Rev. B **76**, 125412 (2007).
[40] C. R. Henry, Prog. Surf. Sci. **80**, 92 (2005).
[41] C. Revenant, F. Leroy, R. Lazzari, G. Renaud, and C. R. Henry, Phys. Rev. B **69**, 035411 (2004).
[42] D. Babonneau, D. Lantiat, S. Camelio, J. Toudert, L. Simonot, F. Pailloux, M.-F. Denanot, and T. Girardeau, Eur. Phys. J.: Appl. Phys. **44**, 3 (2008).
[43] C. R. Henry, Surf. Sci. Rep. **31**, 231 (1998).
[44] C. T. Campbell, Surf. Sci. Rep. **27**, 1 (1997).
[45] J. A. Venables, G. D. T. Spiller, and M. Hanbucken, Rep. Prog. Phys. **47**, 399 (1984).